**Showing research from Physical Science & Engineering (PSE), King Abdullah University of Science and Technology, Saudi Arabia.**

Single crystals of organometallic manganese halides as sustainable high-luminescence materials for X-ray scintillation

Two lead-free hybrid halide crystals, methyl triphenyl phosphonium manganese(II) chloride and phenyltrimethylammonium manganese(II) chloride, are presented. These crystals, grown sustainably *via* solution processing, exhibit remarkable properties, including high photoluminescence quantum yields, strong green emissions, large Stoke shifts, and impressive scintillation yields. A flexible X-ray scintillator screen developed using a composite of poly(methyl methacrylate) and crystal powder achieved a high spatial resolution, demonstrating their potential as an eco-friendly, high-performance material for advanced X-ray imaging applications. Artwork by Maria Joao Castro.
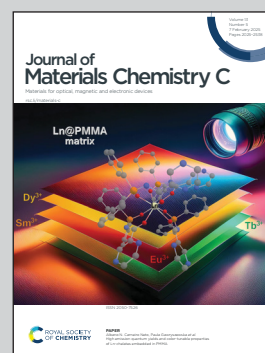
ROYAL SOCIETY
OF **CHEMISTRY**

rsc.li/materials-c

Check for updates

Single crystals of organometallic manganese halides as sustainable high-luminescence materials for X-ray scintillation†

Azimet A. Karluk,[abc] Simil Thomas,[b] Aleksander Shkurenko,[b] Bashir E. Hasanov,[c] Javeed Mahmood, *[abc] Mohamed Eddaoudi *[b] and Cafer T. Yavuz *[abc]

The instability and toxicity of lead halide perovskites hinder their widespread application, despite their potential as novel X-ray materials. Organic-metal halide hybrids are promising luminescent materials with exceptional properties and low-temperature processing for cost-effective, eco-friendly, and high-performance alternatives. Here, we present lead-free, zero-dimensional hybrid halides, methyl triphenyl phosphonium manganese(II) chloride (($MTP)_2MnCl_4$) and phenyltrimethylammonium manganese(II) chloride (($PTA)_2MnCl_4$), grown sustainably by solution processing, in the form of large aggregated single crystals. The crystals have exceptionally high photoluminescence quantum yields of approximately 74.61% and 72.62%, showing strong green emission peaks at 512 nm and 525 nm, respectively. The crystalline materials featured 160 nm and 175 nm Stokes shifts, 40 840 and 29 500 photons per MeV high scintillation yields, and 144.65 and 594.06 nGy s^{-1}, exceptional detection limits, respectively, revealing a self-absorption-free nature. Proving practical value, a flexible X-ray scintillator screen from a composite of poly(methyl methacrylate) and ($MTP)_2MnCl_4$ powder achieved an outstanding spatial resolution of 20 lp per mm, further cementing their viability as X-ray scintillators by being both environmentally friendly and highly effective.

Introduction

X-ray imaging is a popular non-invasive medical imaging technique that uses high-energy electromagnetic radiation to create images of internal body structures. It is also used in a variety of fields, including but not limited to security inspection, space exploration, and scientific research.[1–4] The ability of scintillator-based X-ray imaging systems to convert X-rays into visible light that can be detected by cameras or photodetectors enables high sensitivity and potentially high resolution imaging, making them ideal for medical and scientific imaging.[5,6] Most of the commercially available scintillators are made from inorganic crystals. The production process requires high temperatures under vacuum

over an extended period of time. Several single-crystal scintillators such as $Bi_4Ge_3O_{12}$ (BGO), $Lu_3A_5O_{12}{}^{3+}$ (LuAG), and CsI are proposed for X-ray detection due to their high light yield, reduced light cross-talk, and strong X-ray stopping power. However, these scintillators are limited by the demanding and lengthy manufacturing processes, hindering their broad commercial applications.[7–9] The pursuit of cost-effective and high-performance scintillation materials remains critical for both scientific research and practical applications.

Lead halide perovskites, such as crystalline Formamidinium$PbBr_3$ and nanocrystalline $CsPbBr_3$, have recently emerged as highly sought-after scintillator materials owing to their high atomic number, superior X-ray sensitivity, tunable light emission, low detection limit, fast response time, and ease of solution processability.[10–15] Despite these advantages, lead-based halide perovskites are not without their environmental hazards because of the toxicity of lead, poor moisture stability and high temperature synthesis requirements.[16,17] As a result, research on lead-free perovskites and hybrids is ongoing in an attempt to lessen the impact of these drawbacks. For instance, X-ray imaging applications can benefit from the luminescent properties and low self-absorption of certain low-dimensional perovskites, such as Cs_2Ag-$BiBr_6$,[18] $Cs_3Cu_2I_5$,[19] and $(C_8H_{17}NH_3)_2SnBr_4$.[20]

Environmentally friendly organic manganese halides have recently attracted a lot of attention because of their excellent

a Oxide & Organic Nanomaterials for Energy & Environment (ONE) Laboratory, Physical Science & Engineering (PSE), King Abdullah University of Science and Technology (KAUST), Thuwal 23955, Saudi Arabia.
E-mail: javeed.mahmood@kaust.edu.sa, cafer.yavuz@kaust.edu.sa

b Advanced Membranes & Porous Materials (AMPM) Center, Physical Science & Engineering (PSE), King Abdullah University of Science and Technology (KAUST), Thuwal 23955, Saudi Arabia. E-mail: mohamed.eddaoudi@kaust.edu.sa

c KAUST Catalysis Center (KCC), Physical Science & Engineering (PSE), King Abdullah University of Science and Technology (KAUST), Thuwal 23955, Saudi Arabia

† Electronic supplementary information (ESI) available. CCDC 2353441 and 2353443. For ESI and crystallographic data in CIF or other electronic format see DOI: https://doi.org/10.1039/d4tc03717k

photoelectric properties, high photoluminescence quantum yields, and remarkable stability. Examples of 0D lead-free halide hybrid scintillators include $(C_{40}H_{38}P_2)MnBr_4$,[21] $(C_{38}H_{34}P_2)MnBr_4$,[22] $(C_8H_{20}N)_2MnBr_4$,[23] $(C_8H_{20}N)_2MnI_4$,[24] $(C_{16}H_{36}N)_2MnCl_4$, $(C_8H_{20}ClN)_2MnCl_4$,[25] and $(C_{16}H_{36}N)MnBr_4$.[26] In particular, the 0D versions $(C_{38}H_{34}P_2)MnBr_4$[22] and $(C_{16}H_{36}N)MnBr_4$[26] exhibit promising X-ray detection capabilities, with a high light yield of $\sim 80\,000$ photons per MeV, a low detection limit of 72.8 $nGy_{air}\ s^{-1}$, and 68 000 photons per MeV and yielding 63.3 $nGy_{air}\ s^{-1}$,[26] respectively. However, to our knowledge, there have been limited reports on the utilization of Mn-based halides for flexible X-ray scintillators with high spatial resolution.[26–29] In addition, the varied and adaptable crystal arrangement, along with the potential for efficient light emission, motivated us to further investigate novel 0D hybrid manganese halides that offer strong stability as foundational components for X-ray detectors, with excellent spatial precision.

This work presents the synthesis of two zero-dimensional manganese(II) halide species, methyl triphenyl phosphonium manganese(II) chloride $((MTP)_2MnCl_4)$ and phenyltrimethylammonium manganese(II) chloride $((PTA)_2MnCl_4)$, at low temperature (below 80 °C), which show high performance and excellent reproducibility through a simple solvent evaporation crystallization method. These organic–inorganic halides display bright green emission peaks at 512 nm $((MTP)_2MnCl_4)$ and 525 nm $((PTA)_2MnCl_4)$, with photoluminescence quantum yields (PLQY) of approximately 74.61% and 72.62%, respectively. Moreover, these organic manganese(II) halide hybrids feature self-absorption-free, large Stokes shifts (160 and 175 nm) and excellent scintillation yield properties (40 840 and 29 500 photons per MeV)

with excellent detection limit (144.65 and 594.06 $nGy\ s^{-1}$) characteristics. We also fabricated a flexible, environmentally friendly X-ray scintillator screen using a combination of PMMA and $(MTP)_2MnCl_4$ powder, with a high spatial resolution of 20 lp per mm and a high optical output.

Results and discussion

The two organic manganese(II) halide crystals are synthesized using a simple solvent evaporation process. Crystalline $(MTP)_2MnCl_4$ (**1**) has been obtained by slowly diffusing diethyl ether into a dichloromethane precursor solution containing MTPCl and $MnCl_2$ at room temperature. To prepare $(PTA)_2MnCl_4$ (**2**), 4 ml of deionized water was required to dissolve PTACl and $MnCl_2$ in a 2:1 ratio. The mixture was then allowed to evaporate slowly at 75 °C overnight. More information about the purification and synthesis processes can be found in supplementary methods and Fig. S1 and S2, ESI.† Upon evaporation, large crystalline aggregates (Fig. 1) were grown, with dimensions of approximately $9 \times 3 \times 2$ mm and $4 \times 2 \times 2$ mm, respectively.

When exposed to 365 nm UV light, crystals **1** and **2** produce bright green light. Fig. 1c and d illustrate the crystal structures of **1** and **2**, which were determined using single-crystal X-ray diffraction (SCXRD) analysis. $(MTP)_2MnCl_4$ (**1**) crystallizes in the cubic space group $P2_13$; $(PTA)_2MnCl_4$ (**2**) crystallizes in the monoclinic space group $C2/c$. The average Mn–Cl distances for crystals **1** and **2** are 2.37 Å and 2.36 Å, respectively. The average Cl–Mn–Cl bond angle for both crystals is 109.5°. These anions
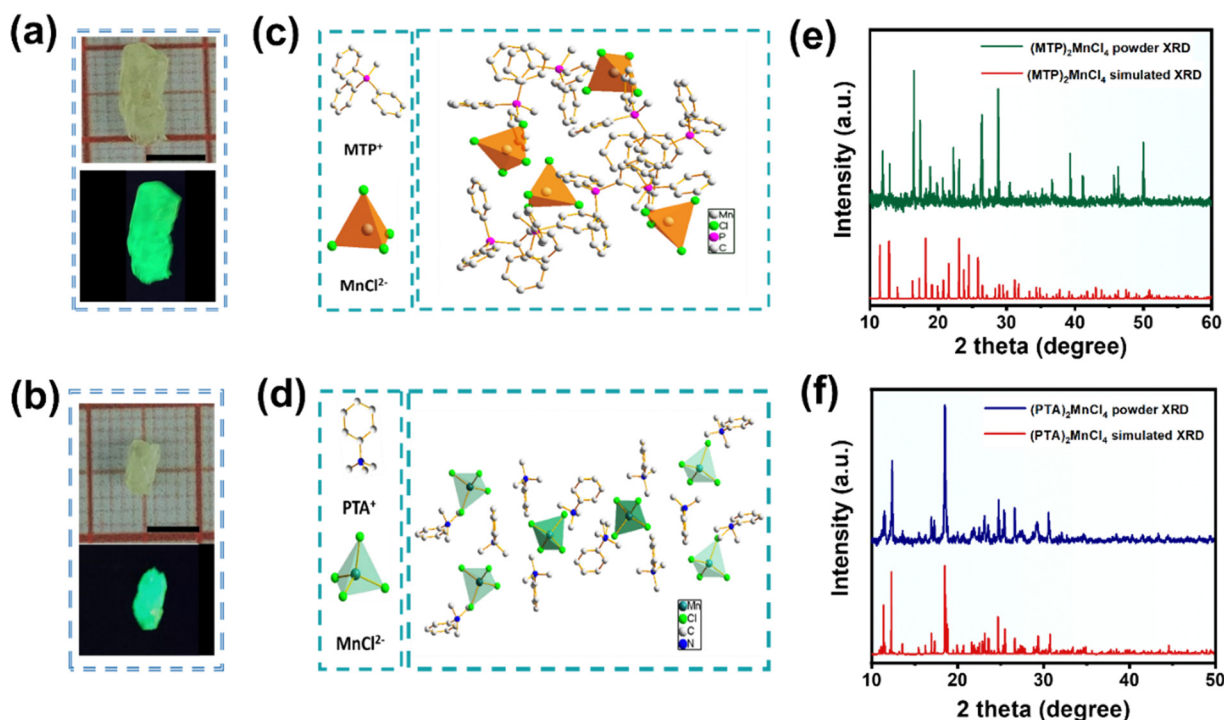
Fig. 1 Digital photographs and single crystal structures. As-grown (a) $(MTP)_2MnCl_4$ and (b) $(PTA)_2MnCl_4$ crystal samples under daylight and ultraviolet light (scale bar: 1 cm). Cation, anion, and crystal structures of (c) $(MTP)_2MnCl_4$ and (d) $(PTA)_2MnCl_4$ crystals. Experimental and SCXRD-based simulated PXRD patterns of (e) $(MTP)_2MnCl_4$ and (f) $(PTA)_2MnCl_4$ crystals.

2166 | *J. Mater. Chem. C*, 2025, **13**, 2165–2171

This journal is © The Royal Society of Chemistry 2025

participate in electrostatic interactions with the bulky $[MTP]^+$ and $[PTA]^+$ cations that surround them, resulting in a zero-dimensional (0D) structure at the molecular level. Additionally, SCXRD analysis shows that 6.5% Cl^- in the crystal structure of **1**, which suggests that 6.5% of $\{MnCl_4\}$ entity is actually $[Mn(III)Cl_4]^-$. Tables S1 and S2, (ESI†) present detailed SCXRD data for crystals **1** and **2**. The powder XRD (PXRD) patterns obtained from crystals **1** and **2** matched the simulated results generated from the SCXRD data (Fig. 1e and f). This observation implies that the as-synthesized crystals have high phase purity. Even after three months of exposure to air, the PXRD patterns of both **1** and **2** showed no changes (Fig. S3, ESI†). Furthermore, the thermal stability of both crystals was evaluated by thermogravimetric analysis (TGA) under inert conditions in nitrogen (N_2) flow. The TGA curves (Fig. S4, ESI†) demonstrate that the samples exhibited remarkable thermal stability when subjected to temperatures below 365 °C for crystal **1** and 205 °C for crystal **2**.

Optical properties

In order to examine the optical characteristics of the 0D single crystals, various techniques, such as steady-state PL, PLE, UV-Vis absorption, and time-correlated single-photon counting, were employed. The comparison of the absorption bands and excitation spectra of crystals **1** and **2** revealed peaks at 298, 360, and 380 nm for crystal **2** and 298, 356 and 378 nm for crystal **1**, respectively. In the UV range of 300–400 nm in the PL excitation spectrum, both crystals showed a dominant peak at 358 nm, which produced a Gaussian-shaped broadband emission. In PL spectra, crystal **1** has a maximum wavelength of 512 nm and crystal **2** has a maximum wavelength of 524 nm (Fig. 2a and Fig. S5, ESI†).

The tetrahedral coordination of the Mn^{2+} ion causes bright green emissions from d–d transitions ($^6A_1 \rightarrow {}^4T_1$) in both crystals of **1** and **2**.[23] The full width at half maximum of crystal **1** is 54 nm, with a Stokes shift of 160 nm, and for crystal **2** it is 52 nm, with a Stokes shift of 175 nm (Fig. 2a and Fig. S5, ESI†). The PL contour mappings shown in Fig. 2b and Fig. S6, ESI† reveal that both crystals have a single emission center. PL decay curves of crystals **1** and **2** reveal bi-exponential decay with decay times of 1.97 ms and 3.45 ms, respectively (Fig. 2c). These similarities in curve shape and decay times in the millisecond range further confirm the Mn^{2+} ion's characteristic $^6A_1$ to $^4T_1$ transition as the origin of the emission.[23]

Single crystals of **1** and **2** record high PLQY of 74.61% and 72%, respectively (Fig. S7 and S8, ESI†). The high PLQY is attributed to crystal framework construction facilitated by large organic cations, which elongate Mn–Mn distances and effectively suppress non-radiative energy dissipation, such as thermal vibrations of inorganic anions.[30,31] Both crystals were subjected to temperature-dependent photoluminescence spectral analysis to probe the photophysical characteristics and electron–phonon interactions of the 0D organic manganese halides (Fig. 2d and Fig. S9, ESI†). The presence of a single emission band at all temperatures in crystal **1** suggests that the emission originates from the same excited states. Remarkably, the integrated intensity of the photoluminescence for crystal **1** increased gradually from 100 to 358 K and then decreased once the temperature exceeded 358 K. This is due to the increased softening of the organic framework as the temperature increases from 100 to 358 K, resulting in a higher thermal activation energy for free excitons. This allows them to cross the
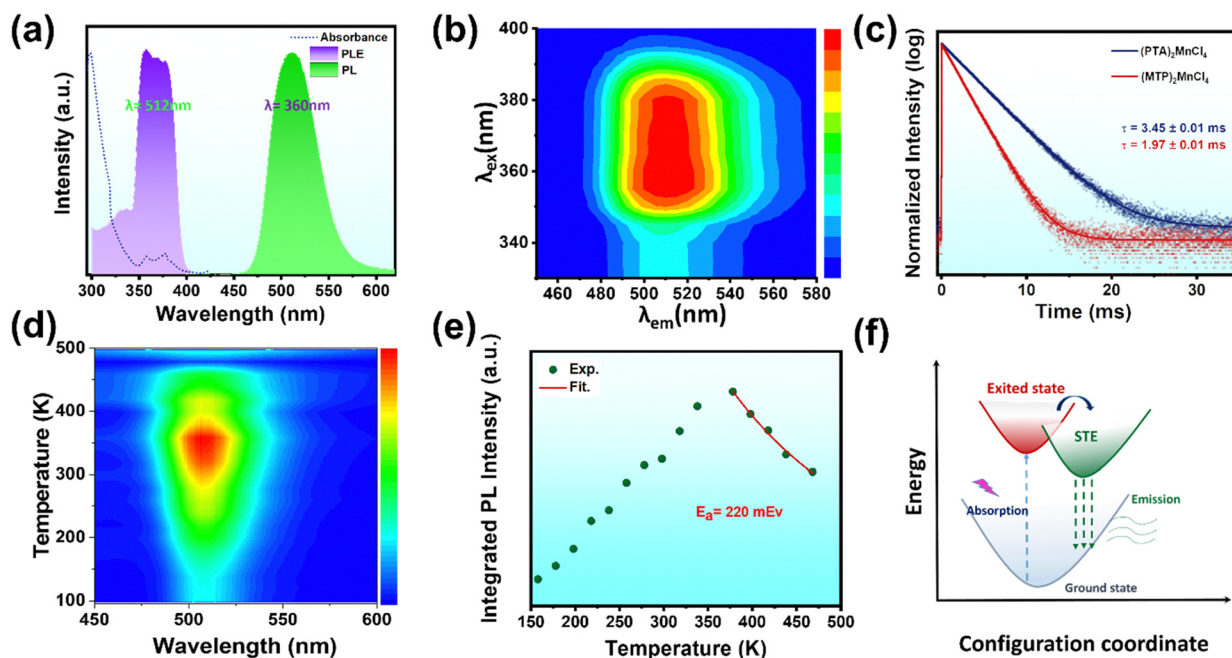
Fig. 2 Optical evaluation of the samples (a) absorbance, PL excitation and emission spectra of $(MTP)_2MnCl_4$ and (b) color mapping of the consecutive 3D PL spectrum of $(MTP)_2MnCl_4$. (c) PL decay curves at 300 K for $(MTP)_2MnCl_4$ and $(PTA)_2MnCl_4$. (d) Color mapping of temperature-dependent PL emission spectra, (e) experimental and fitted emission intensity *vs.* temperature, (f) carrier transition pathway and PL mechanism of $(MTP)_2MnCl_4$.

This journal is © The Royal Society of Chemistry 2025

J. Mater. Chem. C, 2025, **13**, 2165–2171 | **2167**

potential barrier and accumulate in the self-trapped exciton (STE) state, resulting in a strong STE emission. However, beyond 358 K, the photoluminescence intensity is thermally quenched due to thermally activated non-radiative recombination processes.[32,33] The thermal activation energy (E_a) plays a crucial role in the excitation and recombination processes. To evaluate the thermal activation energy of emission quenching above 358 K, the following equation can be employed.

$$I_{PL} = \frac{I_0}{1 + A \times \exp\left(\frac{-E_a}{k_B \times T}\right)}$$

The E_a was determined to be 220 meV for crystal **1** and 44 meV for crystal **2** using the equation, where I_0 represents the low-temperature photoluminescence intensity, k_B is the Boltzmann constant, and A is the ratio between the radiative and non-radiative decay rates. The calculated E_a values of both crystals are notably higher than the thermal energy (26 meV) of free excitons at room temperature, as well as the thermal energies of 3D perovskites and other hybrid halides.[32,34] The photoluminescence peak position of crystal **1** varies only slightly (Fig. S10a, ESI†), which is consistent with observations in other materials based on the STE states.[19] The photoluminescence intensity in crystal **2** decreased as the temperature increased from 100 to 238 K. However, as the temperature rises, the luminescence intensity increases again, accompanied by a blue shift in the peak position (Fig. S9 and S10, ESI†), which can be attributed to acoustic phonon-exciton interaction and lattice expansion.[35] The initial stage of intensity decrease is caused by temperature quenching, which is common in luminescent materials. The subsequent stage can be attributed to isolated luminescence centers with larger Mn–Mn distances, inhibiting energy migration with increasing temperature.[36,37]

To gain a deeper insight into the electronic structures of the crystals **1** and **2** density functional theory (DFT) calculations were carried out. The valence band maximum (VB_{max}) and conduction band minimum (CB_{min}) of the two 0D organic manganese halides are nearly flat, as shown in Fig. 3a and c, which indicates that these electronic states are highly localized.

The electronic couplings between nearby $MnCl_4$ tetrahedra of both **1** and **2** are small because of the large distance between the adjacent inorganic $MnCl_4$ clusters. This is consistent with the partial charge density plot of the VB_{max} and CB_{min} for the manganese halides (Fig. 3b and d). The density of states (DOS) of both manganese halides shows that the VB_{max} consists of Mn 3d and Cl 3p orbitals, whereas the CB_{min} consists of orbitals from the organic unit (Fig. 3a and c). These results indicate that the band absorption of manganese halides mainly originates from the charge transfer from the inorganic $MnCl_4$ cluster to its organic counterpart. The DFT calculated band gaps for **1** and **2** are 3.06 and 3.61 eV, respectively. These results are also further confirmed with the Tauc plot from absorption spectra of **1** and **2**, which are 3.3 and 3.6 eV (Fig. S14, ESI†).

The high PLQY and significant Stokes shift observed in crystals **1** and **2** motivated further investigation of their potential as X-ray scintillators. They were tested against commercially available $Bi_4Ge_3O_{12}$ (BGO) to determine their performances. The RL emission spectra of crystals **1** and **2** and BGO were recorded at room temperature using X-ray radiation at a power of 30 kV and a current of 30 µA. The RL spectra exhibit
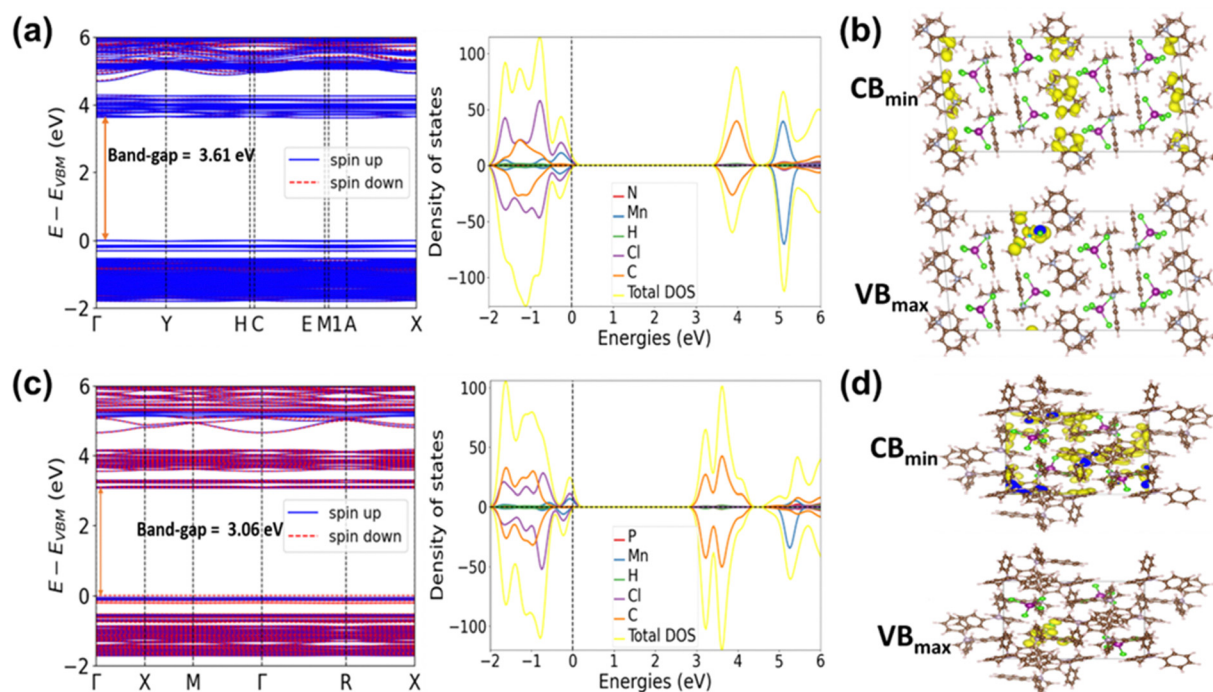

Fig. 3 Electronic band structures and DOS of (a) $(PTA)_2MnCl_4$ (c) $(MTP)_2MnCl_4$. VB_{max} and CB_{min} associated partial charge density contours of (b) $(PTA)_2MnCl_4$ and (d) $(MTP)_2MnCl_4$.

2168 | *J. Mater. Chem. C*, 2025, **13**, 2165–2171

This journal is © The Royal Society of Chemistry 2025

characteristics similar to those of the corresponding PL spectra (Fig. 4a). Considering the irradiation area of the emission spectrum, crystal **1** demonstrated the highest RL response with a light yield of 40 840 photons per MeV, while crystal **2** exhibited a light yield of 29 500 photons per MeV. These values are 4.8 and 2.9 times higher than that of BGO, respectively.

The light yields of **1** and **2** were further investigated using cerium-doped lutetium yttrium orthosilicate (LYSO) as a reference (Fig. S15, ESI†). The scintillation yields of crystals **1** and **2** surpassed those of many 0D hybrid organometallic halides, including $(C_8H_{20}N)_2MnBr_4$ (24 400 photon per MeV),[23] $(TBA)_2MnCl_4$ (21 000 photon per MeV),[25] and $(PPN)_2SbCl_5$ (17 000 photon per MeV).[38] They also outperformed certain commercial scintillators, such as LYSO (33 200 photons per MeV) and $CdWO_4$ (28 000 photons per MeV) (Fig. 4e). To determine the X-ray detection limit, RL emission spectra were recorded at various dose rates (64–650 $Gy_{air}\ s^{-1}$) (Fig. 4b and c). The RL intensity was positively correlated with the X-ray dose rate (Fig. 4b). Linear fitting yielded a low detection limit of 144.65 $nGy_{air}\ s^{-1}$ and 594.06 $nGy_{air}\ s^{-1}$ at a signal-to-noise ratio

of 3 for crystals **1** and **2**, respectively. These values are approximately 38 times and 9 times lower than the dose rate required for X-ray diagnostics (5.5 $\mu Gy_{air}\ s^{-1}$).[39] Temperature-dependent RL intensity measurements were conducted for crystal **1** (see Fig. S19, ESI†). As expected, the RL emission intensity increased with rising temperature, reflecting the behavior observed in PL. After an extended period of continuous X-ray irradiation at a dose rate of 9.7 $mGy_{air}\ s^{-1}$, the RL emission intensity of the crystal **1** was monitored in order to evaluate its RL stability under X-ray excitation (Fig. 4d). Despite a total X-ray dose of 58.2 $mGy_{air}\ s^{-1}$, crystal **1** exhibited stable RL emission with a negligible decrease in intensity, indicating a high X-ray tolerance. The practical application of **1** as a scintillator was validated by X-ray imaging using a homemade X-ray imaging setup (Fig. 4f).

For practical considerations, a scintillator film with a thickness of 80 μm and a surface area of 20 cm^2 was fabricated by drop casting **1** powder mixed with a PMMA binder (Fig. 4g and Fig. S11, ESI†). The scintillator film exhibits excellent imaging capabilities, as confirmed by X-ray imaging using standard
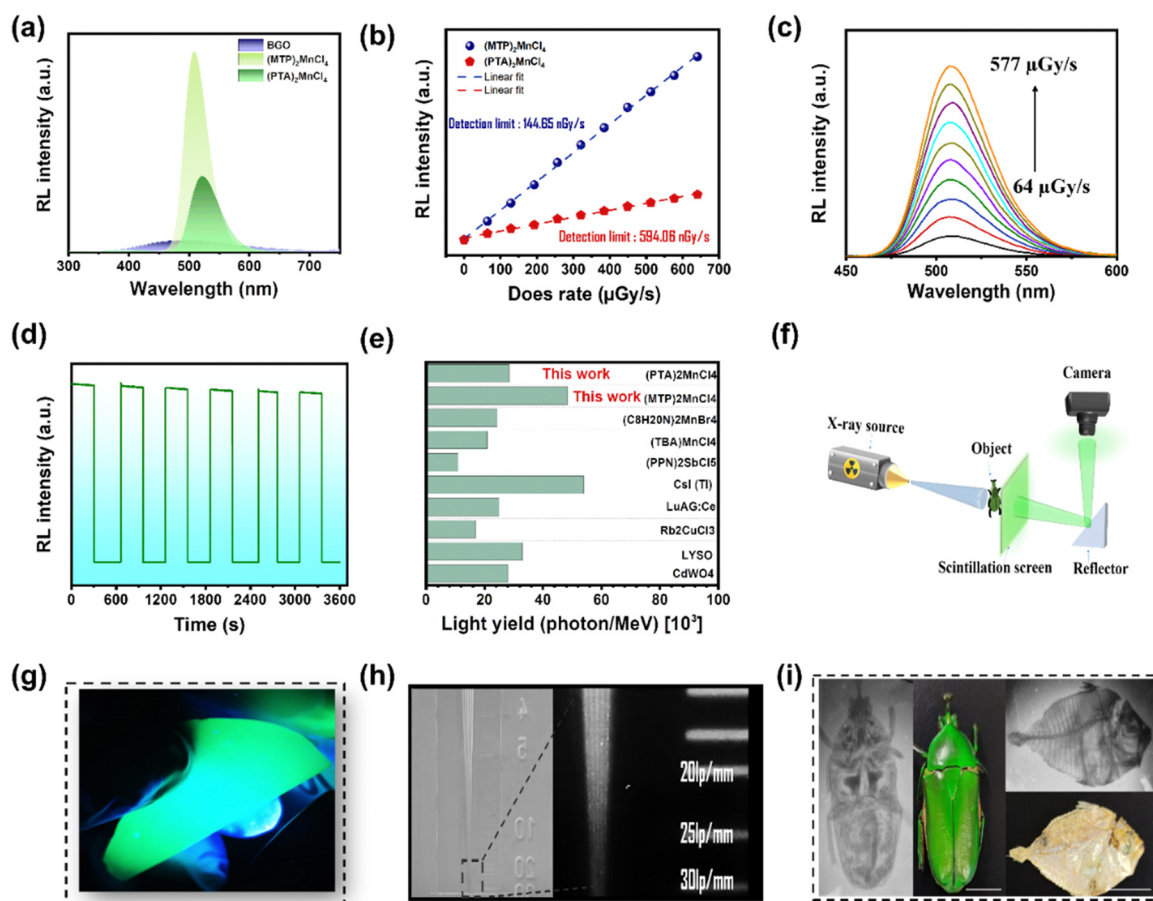
Fig. 4 (a) X-ray excited radioluminescence (RL) spectra of crystals **1**, **2**, and BGO under 30 kV and 30 μA X-ray excitation. (b) The detection limit (DL) of crystal **1** (blue line) and crystal **2** (Red line). (c) Dose-rate-dependent RL spectra of crystal **1**. (d) RL emission intensity under constant X-ray irradiation (e) Comparison of scintillator light yields of crystal **1**, **2** and previously reported and commercially available scintillators. (f) The schematic of a homemade X-ray imaging system. (g) Photographs of flexible $(MTP)_2MnCl_4$ powder @PMMA-10% film under UV light. (h) The spatial resolution of the 80 μm $(MTP)_2MnCl_4$ powder @PMMA-10% film was determined by a standard line-pair card (lp per mm). (i) Photograph and X-ray image of Scarab beetle and fish (scale bar: 1 cm^{-1}).

This journal is © The Royal Society of Chemistry 2025

J. Mater. Chem. C, 2025, **13**, 2165–2171 | **2169**

X-ray resolution test panels. The observed limit was approximately 20 lp per mm and the intensity profile had a high resolution of 116 μm (Fig. 4h and Fig. S12, ESI†). Under X-ray irradiation, Fig. 4i and Fig. S13, ESI,† clearly show the recognition of scarab beetle and fish bones, as well as the metal part of a ballpoint pen. We also observed a gradual decrease in the clarity of the X-ray image of the scarab beetle as we applied different X-ray powers (ranging from 50 kV 20 μA to 120 μA) (Fig. S16, ESI†). The spatial resolution of our scintillator film surpasses that of most scintillators fabricated with 0D organometallic halides, $(C_8H_{20}N)_2MnBr_4$ and $C_4H_{12}NMnCl_3$ (5 lp per mm),[23] $(C_{24}H_{20}P)_2MnBr_4$ (14.5 lp per mm),[28] $(TBA)_2MnCl_4$ (5.6 lp per mm),[25] $(ETP)_2MnBr_4$ (13 lp per mm),[40] indicating the outstanding X-ray scintillation performance of these hybrid manganese chloride materials and their potential applications in medical imaging, X-ray detection, radiography, non-destructive testing, and radiation monitoring.

Conclusion

We successfully synthesized two 0D hybrid manganese chlorides, $(MTP)_2MnCl_4$ and $(PTA)_2MnCl_4$, using a simple solvent-evaporation and non-solvent crystallization method. These compounds exhibit bright green photoluminescence with a high quantum yield and strong radioluminescence emission. They have excellent light output, a low detection limit, and a high tolerance to hard X-rays, making them ideal for high-resolution X-ray radiography and imaging applications. Furthermore, they have the advantages of low-cost, eco-friendly synthesis, easy preparation and processing, and high environmental stability. These features distinguish them from other 3D all-inorganic metal halide scintillators and position them as promising candidates for future scintillation technologies.

Data availability

The data supporting this article have been included as part of the ESI.†

Conflicts of interest

There are no conflicts to declare.

Acknowledgements

Notes and references

1 Y. Wang, X. Yin, W. Liu, J. Xie, J. Chen, M. A. Silver, D. Sheng, L. Chen, J. Diwu and N. Liu, *Angew. Chem., Int. Ed.*, 2018, **130**, 8009–8013.

2 H. Wei and J. Huang, *Nat. Commun.*, 2019, **10**, 1066.

3 T. J. Hajagos, C. Liu, N. J. Cherepy and Q. Pei, *Adv. Mater.*, 2018, **30**, 1706956.

4 X. Ou, X. Qin, B. Huang, J. Zan, Q. Wu, Z. Hong, L. Xie, H. Bian, Z. Yi and X. Chen, *Nature*, 2021, **590**, 410–415.

5 M. Nikl and A. Yoshikawa, *Adv. Opt. Mater.*, 2015, **3**, 463–481.

6 B. K. Cha, J. Y. Kim, T. J. Kim, C. Sim and G. Cho, *Radiat. Meas.*, 2010, **45**, 742–745.

7 M. Yao, J. Jiang, D. Xin, Y. Ma, W. Wei, X. Zheng and L. Shen, *Nano Lett.*, 2021, **21**, 3947–3955.

8 O. D. Moseley, T. A. Doherty, R. Parmee, M. Anaya and S. D. Stranks, *J. Mater. Chem. C*, 2021, **9**, 11588–11604.

9 B. K. Cha, J.-H. Shin, J. H. Bae, C.-H. Lee, S. Chang, H. K. Kim, C. K. Kim and G. Cho, *Nucl. Instrum. Methods Phys. Res., Sect. A*, 2009, **604**, 224–228.

10 Q. Chen, J. Wu, X. Ou, B. Huang, J. Almutlaq, A. A. Zhumekenov, X. Guan, S. Han, L. Liang and Z. Yi, *Nature*, 2018, **561**, 88–93.

11 Y. Zhang, R. Sun, X. Ou, K. Fu, Q. Chen, Y. Ding, L.-J. Xu, L. Liu, Y. Han and A. V. Malko, *ACS Nano*, 2019, **13**, 2520–2525.

12 J. H. Heo, D. H. Shin, J. K. Park, D. H. Kim, S. J. Lee and S. H. Im, *Adv. Mater.*, 2018, **30**, 1801743.

13 V. B. Mykhaylyk, H. Kraus and M. Saliba, *Mater. Horiz.*, 2019, **6**, 1740–1747.

14 W. Shao, Y. Li, X. Wang, X. Ouyang, J. Cai, C. Li, X. Ouyang, Z. Wu and Q. Xu, *Phys. Chem. Chem. Phys.*, 2020, **22**, 6970–6974.

15 F. Maddalena, A. Xie, X. Y. Chin, R. Begum, M. E. Witkowski, M. Makowski, B. Mahler, W. Drozdowski, S. V. Springham and R. S. Rawat, *J. Phys. Chem. C*, 2021, **125**, 14082–14088.

16 S. Huang, H. Yi, L. Zhang, Z. Jin, Y. Long, Y. Zhang, Q. Liao, J. Na, H. Cui and S. Ruan, *J. Hazard. Mater.*, 2020, **393**, 122324.

17 W. Zhu, W. Ma, Y. Su, Z. Chen, X. Chen, Y. Ma, L. Bai, W. Xiao, T. Liu and H. Zhu, *Light: Sci. Appl.*, 2020, **9**, 112.

18 W. Pan, B. Yang, G. Niu, K. H. Xue, X. Du, L. Yin, M. Zhang, H. Wu, X. S. Miao and J. Tang, *Adv. Mater.*, 2019, **31**, 1904405.

19 L. Lian, M. Zheng, W. Zhang, L. Yin, X. Du, P. Zhang, X. Zhang, J. Gao, D. Zhang and L. Gao, *Adv. Sci.*, 2020, **7**, 2000195.

20 J. Cao, Z. Guo, S. Zhu, Y. Fu, H. Zhang, Q. Wang and Z. Gu, *ACS Appl. Mater. Interfaces*, 2020, **12**, 19797–19804.

21 T. Xu, W. Li, Z. Zhou, Y. Li, M. Nikl, M. Buryi, J. Zhu, G. Niu, J. Tang and G. Ren, *Phys. Status Solidi RRL*, 2022, **16**, 2200175.

22 L.-J. Xu, X. Lin, Q. He, M. Worku and B. Ma, *Nat. Commun.*, 2020, **11**, 4329.

23 T. Jiang, W. Ma, H. Zhang, Y. Tian, G. Lin, W. Xiao, X. Yu, J. Qiu, X. Xu and Y. Yang, *Adv. Funct. Mater.*, 2021, **31**, 2009973.

24 Z.-Z. Zhang, J.-H. Wei, J.-B. Luo, X.-D. Wang, Z.-L. He and D.-B. Kuang, *ACS Appl. Mater. Interfaces*, 2022, **14**, 47913–47921.

2170 | *J. Mater. Chem. C*, 2025, **13**, 2165–2171

This journal is © The Royal Society of Chemistry 2025

25 S. Cao, C. Li, P. He, J. A. Lai, K. An, M. Zhou, P. Feng, M. Zhou and X. Tang, *ACS Appl. Opt. Mater.*, 2023, **1**, 623–632.

26 W. Ma, D. Liang, Q. Qian, Q. Mo, S. Zhao, W. Cai, J. Chen and Z. Zang, *eScience*, 2022, **3**, 100089.

27 W. Shao, G. Zhu, X. Wang, Z. Zhang, H. Lv, W. Deng, X. Zhang and H. Liang, *ACS Appl. Mater. Interfaces*, 2023, **15**, 932–941.

28 K. Xia, P. Ran, W. Wang, J. Yu, G. Xu, K. Wang, X. Pi, Q. He, Y. Yang and J. Pan, *Adv. Opt. Mater.*, 2022, **10**, 2201028.

29 S. Ji, Y. Liu, Y. Wang, H. Zhao, Q. Wang, Q. Meng, Y. Bai, J. Jiang, Q. Shen and F. Liu, *Cryst. Growth Des.*, 2024, **24**, 2094–2103.

30 L. Mao, P. Guo, S. Wang, A. K. Cheetham and R. Seshadri, *J. Am. Chem. Soc.*, 2020, **142**, 13582–13589.

31 Y. Wu, W. Fan, Z. Gao, Z. Tang, L. Lei, X. Sun, Y. Li, H.-L. Cai and X. Wu, *Nano Energy*, 2020, **77**, 105170.

32 H. Peng, S. Yao, Y. Guo, R. Zhi, X. Wang, F. Ge, Y. Tian, J. Wang and B. Zou, *J. Phys. Chem. Lett.*, 2020, **11**, 4703–4710.

33 C. Zhou, H. Lin, J. Neu, Y. Zhou, M. Chaaban, S. Lee, M. Worku, B. Chen, R. Clark and W. Cheng, *ACS Energy Lett.*, 2019, **4**, 1579–1583.

34 Y. Jiang, X. Wang and A. Pan, *Adv. Mater.*, 2019, **31**, 1806671.

35 M. Zou, J. Wang, M. S. Khan, A. Mahmood, L. Zhang, Y. Guo, K. Zhang, S. Wang and B. Zou, *Nanotechnology*, 2020, **31**, 325002.

36 G. Zhou, Z. Liu, J. Huang, M. S. Molokeev, Z. Xiao, C. Ma and Z. Xia, *J. Phys. Chem. Lett.*, 2020, **11**, 5956–5962.

37 Y. Zhao, C. Riemersma, F. Pietra, R. Koole, C. de Mello Donegá and A. Meijerink, *ACS Nano*, 2012, **6**, 9058–9067.

38 Q. He, C. Zhou, L. Xu, S. Lee, X. Lin, J. Neu, M. Worku, M. Chaaban and B. Ma, *ACS Mater. Lett.*, 2020, **2**, 633–638.

39 H. Wei, Y. Fang, P. Mulligan, W. Chuirazzi, H.-H. Fang, C. Wang, B. R. Ecker, Y. Gao, M. A. Loi and L. Cao, *Nat. Photonics*, 2016, **10**, 333–339.

40 B. Li, Y. Xu, X. Zhang, K. Han, J. Jin and Z. Xia, *Adv. Opt. Mater.*, 2022, **10**, 2102793.

This journal is © The Royal Society of Chemistry 2025

J. Mater. Chem. C, 2025, **13**, 2165–2171 | **2171**